12th International Symposium on Turbulence and Shear Flow Phenomena (TSFP12)
Osaka, Japan (Online), July 19-22, 2022

DIRECT GLOBAL STABILITY OF ATMOSPHERIC SHEAR FLOW THAT CAUSES AIRCRAFT TURBULENCE

Ryoichi Yoshimura
Graduate School of Engineering
Tohoku University
6-6-01, Aramakiaoba, Sendai, Miyagi, Japan
ryouichi.yoshimura.s2@dc.tohoku.ac.jp

Aiko Yakeno
Institute of Fluid Science
Tohoku University
IFS 2nd building, 2-1-1, Katahira, Sendai, Miyagi, Japan
aiko.yakeno@tohoku.ac.jp

Junshi Ito
Graduate School of Science
Tohoku University
6-3, Aramakiaoba, Sendai, Miyagi, Japan
junshi@tohoku.ac.jp

Shigeru Obayashi
Institute of Fluid Science
Tohoku University
IFS 2nd building, 2-1-1, Katahira, Sendai, Miyagi, Japan
s.obayashi@tohoku.ac.jp

ABSTRACT

We investigate the specific flow transient process in the atmospheric turbulence causing aircraft shaking. On Dec. 30, 2020 over Japan, Kelvin-Helmholtz (KH) waves that occurred in a 3D shear layer, whose momentum thickness was approximately 1-2 [km], broke into three-dimensional vortices smaller than 100 [m] that was responsible for aircraft turbulence. A 3D Euler solver simulates the KH vortices bifurcating at a specific wavelength, and tiny streamwise vortices appearing between bifurcation points trigger turbulence transition. In the analysis, we consider the flow sensitivity on KH vortices by computing a small disturbance growth using the original compressible Euler equations. We set the KH vortices as the initial flow condition, and see the growth of a sinusoidal disturbance. Dependency of the initial amplitude of the disturbance on the growth is also investigated to confirm the nonlinear effects were small. As a result, disturbances do not grow exponentially. The energy growth of the lower frequency disturbances tends to fluctuate in time and relatively stay small, while the others grow monotonically. And we find that the optimal wavelength of the disturbance seems to be closer to the interval at which the KH vortices bifurcate.

INTRODUCTION

According to statistics by Japan Transport and Safety Board (JTSB), more than half of airborne accidents in recent 10 years are due to atmospheric turbulence. In winter Japan, especially Kanto (around Tokyo) region has a lot of air traffic, leading to a lot of encounters with turbulence (pilot report, PIREP) from the free shear layer instability that is induced between north wind near the surface and westerly wind around 4km altitude. There are some studies on turbulence over the Kanto region in winter (Shibata (1968) and Tomine *et al.* (1987)).

Turbulence caused by the free shear instability is not limited to over Japan. The shear instability turbulence can occur under a jet axis under the condition of tropopause folding (Kim & Chun (2010)), over a vertical shear above a jet axis enhanced by convection below (Trier *et al.* (2012)), and above a jet convectively reinforced near a mid-latitude cyclone (Trier *et al.* (2020)).

We need a simple and precise method to forecast the shear instability (KH instability) turbulence that appears in the sky. Japanese operational forecast system for significant weather (FBJP) forecasts the large possibility area of turbulence occurrence based on the Richardson number and other indices and does not forecast information on the precise location and intensity of local turbulence.

It is important to understand processes from shear layer instability to turbulence to propose and construct a new method for turbulence estimation. However, there have been almost no studies that numerically investigated turbulence transition from KH instability waves in the three-dimensional atmospheric field. Several studies have discussed that nonlinear and 3D transition occurring in 2D KH waves triggers turbulence transition of KH waves. Vortex core instability (Bernal & Roshko (1986)) and KH vortices bending due to the rib structure appearing on the braid region (Pierrehumbert & Widnall (1982)) are the possible causes leading to turbulence.

In this study, we investigate processes of KH wave breakings in 3D space from a view point of sensitivity. The vertical wind profiles simulated by an atmospheric simulation is utilized to compute the baseflow, growing KH vortices. Examples of such sensitivity analysis on dynamical systems are an estimation of error growth in an atmospheric simulation (Toth & Kalnay (1993), Roberto *et al.* (2007) and Liu & Kalnay (2008)) and optimal sensor placement based on observability Gramian empirically composed from simulation outputs (Kang & Xu (2012) and Yoshimura *et al.* (2020)). We temporally integrate a small disturbance on KH waves using a three-dimensional Euler solver, to see what wavelength has a large sensitivity to KH waves. This is different from the conventional methods that treat infinite-time responses based on eigenvalue analysis of the dynamical system. For related methods, Mack *et al.* (2008) performed the global linear stability of a 3D flow field around a infinite swept wing, approximating eigenvalues of the field by Krylov subspace composed of outputs of direct numerical simulations.

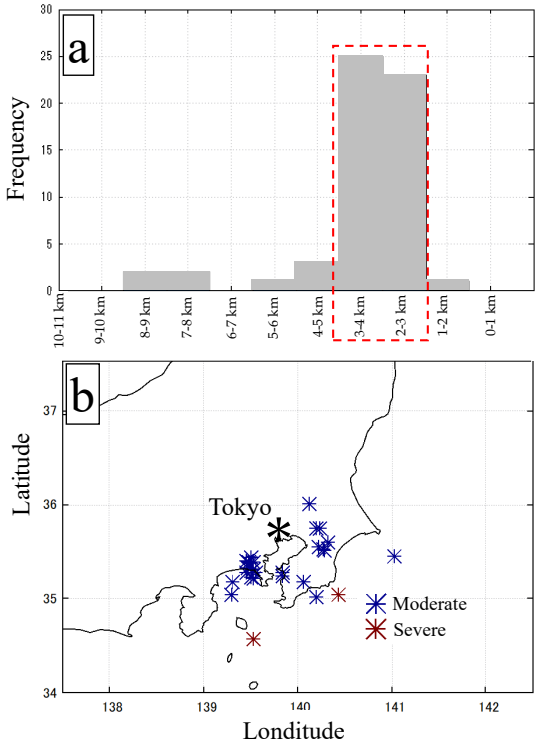

Figure 1. (a) Histogram of the reported height and (b) Horizontal distribution of reports and turbulence intensity

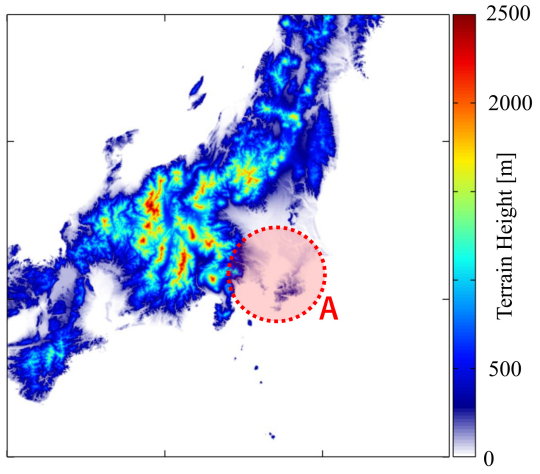

Figure 2. Computational domain for Asuca atmospheric simulation

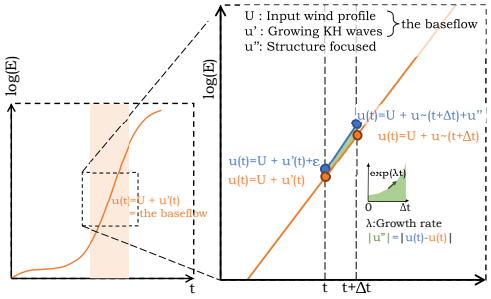

Figure 3. Schematic of Sensitivity Analysis

METHODS

Atmospheric Turbulence Simulation

We used ASUCA (JMA (2019)) to reproduce the atmospheric conditions with turbulence and the baseflow. ASUCA numerically solves the fully compressible non-hydrostatic equations, discretizing with the finite-volume method and the 3rd-order RK. The governing equations are solved on a generalized coordinate system to make the grid points be smoothly along with terrain. Koren's advection scheme was used to suppress unrealistic oscillation. Deardorff SGS model was used for turbulence mixing. Any artificial diffusivity schemes were not used in the simulations. We target the event in which numerous PIREPs were reported around 2-4 km altitude over the south-Kanto region on Dec. 30, 2020. Fig.1 summarizes turbulence encounter reports (PIREPs) reported on the day. Most PIREPs are concentrated on about 3km over the vicinity of Tokyo, suggesting that flights from/to Tokyo well encountered turbulence.

Figure 2 shows the domain configuration. The domain is centered around 139E, 36N, which resolves the region where multiple PIREPs were reported (Area A, Fig.2) with a 500 m horizontal grid spacing. Vertical grid spacing increases linearly from 20m to 100m, remaining 100 m from 1-6 km altitude, and increases to 500 m near 17 km altitude. Japan Meteorological Agency MSM data are used as initial/boundary conditions for the simulation. The simulation is integrated for 9 h from 3:00UTC Dec. 30 to cover the event.

Sensitivity Analysis

A second instability process was investigated by a sensitivity analysis using an in-house Euler solver. This solver discretizes Euler equations on a generalized coordinate system with Compact scheme (Lele (1992)), and time-integrates with TVD-RK (Shu & Osher (1988)). We prepared three grids (S_{small}, $S_{small,hires}$, S_{large}) to see grid resolution (67 m and 33 m) and domain width (40 km and 80 km) influence. All grids have the same vertical grid distribution where the grid interval takes the minimum value of 7 m at the region of the strongest vertical wind shear. We set periodic boundaries in x and y directions and fixed boundaries on top/bottom boundaries.

Figure 3 explains our procedure. As we investigate growing structures on KH vortices, we consider the baseflow, a set of growing KH vortices, to be time-varying. Using the Euler solver, we firstly compute KH vortices $u_i'(x,y,z,t)$ induced on a vertical wind profile with a strong shear $U_i(z)$. We consider $U_i + u_i'$ to be the baseflow in this study. In the right figure of Fig.3, we add a sinusoidal wave u_i'' on the baseflow $U_i + u_i'$ and see its growth. We focus on the energy of the disturbance, which is difference between the the blue plot $U_i + u_i' + u_i''$ and the baseflow $U_i + u_i'$ (the orange plot).

Table 1. Computational Conditions

	N_x, N_y, N_z[pts]	D_x, D_y, D_z(min, max)[m]
S_{small}	601, 601, 253	67, 67, (7, 1200)
$S_{small,hires}$	1202, 1202, 253	33, 33, (7, 1200)
S_{large}	1202, 1202, 253	67, 67, (7, 1200)

RESULTS AND DISCUSSIONS

Atmospheric Turbulence Simulation

Figure 4 suggests that the turbulence over Tokyo on Dec. 30, 2020, was from Kelvin-Helmholtz instability. Fig.4a is the 3 km altitude cross-section of the vertical wind component at 10:00 UTC on Dec. 30, 2020. Wave trains of vertical wind (red/blue stripes) and the shear vectors, vector difference between wind vectors at 4 km and 2.5 km altitudes, are almost perpendicular to each other. These wave trains were moving northeast at the speed of 30 m/s, the speed of wind at 3 km altitude. Fig.4b is the vertical cross-section XX'. Richardson number, which is used as one of the indices of turbulence occurrence, takes its local minimum at around 3km where a large part of PIREPs was reported (Fig.1a). Where PIREPs are located and where KH waves are located are well correlated, suggesting that KH instability caused by the small Richardson number mainly contributed to inducing aircraft turbulence at 3 km altitude. KH waves are visualized on the right side of the figure as the regular waves of potential temperature. Local Richardson number can be estimated by Eq.(1). θ, g, u, and v are potential temperature, acceleration of gravity, and horizontal wind components respectively.

$$Ri = \frac{g}{\theta}\frac{d\theta}{dz} \Big/ \left(\left(\frac{du}{dz}\right)^2 + \left(\frac{dv}{dz}\right)^2 \right) \tag{1}$$

Sensitivity Analysis

Area A in Fig.4a is the region where we obtained the averaged vertical wind profile. Fig.5a shows the averaged profile and Fig.5b is the profile $U_i(z)$ for the sensitivity analysis. We shifted the height of shear and removed the profiles near-surface and upper air to obtain U_i.

Fig.6(a)-(c) are snapshots of KH waves induced on the profile U_i that the Euler solver simulated on S_{small} grid. KH waves are visualized as iso-surfaces of the vertical wind component colored by pressure. KH waves are induced at the frequency between 3 and 4 [waves/Domain width] and the bifurcation frequency of about 2 [bifurcations/Domain width] (Fig.6a), KH waves break around the bifurcation points (Fig.6b) and turbulence transition occurs (Fig.6c). Lines (a) in Fig.7 are the energy of u_i' and its growth rate. From $t = 800$ to 1000 [s], the energy increases linearly until when saturation occurs due to turbulence transition. The initial wind profile U_i was disturbed with white noise, which has a uniform spectrum, to facilitate inducing KH instability. The amplitude of the perturbation was $\varepsilon = 10^{-5}$ [$\times$330 m/s].

Based on the above simulation, we prepare simplified KH vortices, the baseflow, for the sensitivity analysis. Fig.6d shows the baseflow at $t = 1500$ [s] and the direction of the shear, showing that KH waves are almost perpendicular to the shear vector (45 degrees from the x and y axes). The initial condition is the same as the above simulation, except for adding the following sinusoidal waves instead of the white noise to facilitate inducing the almost same wave frequency. To satisfy the periodic boundary conditions, we set exactly 4 [waves/Domain width], 10 km period in the x and y directions, for the initial disturbance.

$$u(z,y,z,t=0) = U(z) + \varepsilon \sin(2\pi(x+y)/(L/4)) \tag{2}$$

The (b) plots in Fig.7 are the energy and the growth rate of the KH vortices, the baseflow. We conducted the sensitivity

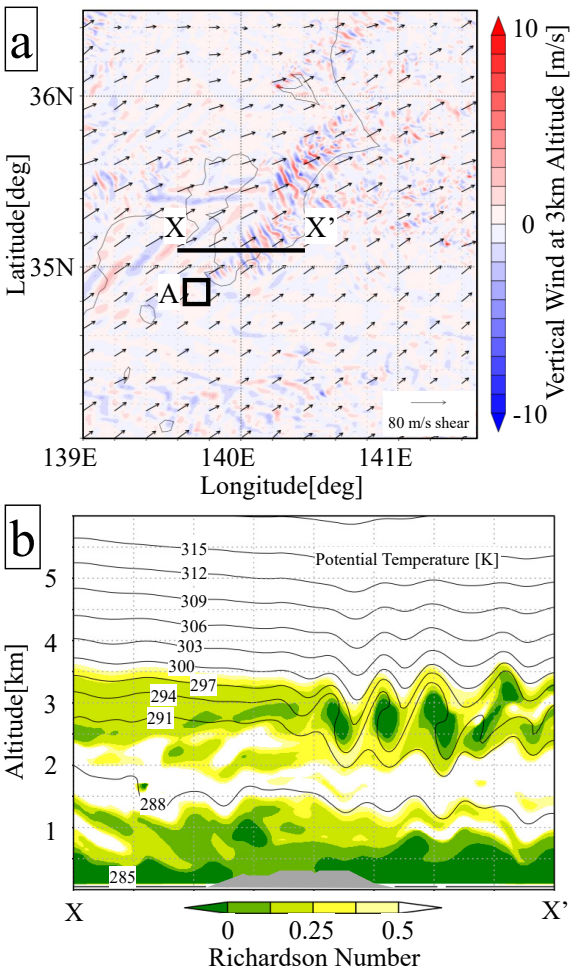

Figure 4. (a) Simulated vertical wind field and shear vectors, and (b) Vertical cross-section X-X' showing potential temperature and Richardson number.

analysis during the period $t = 800 - 1000$ s when KH vortices grow linearly.

We see the wavenumber sensitivity to the baseflow to investigate the KH waves transition. Following Goto & Kawahara (2017), we assume the secondary vortices whose direction is perpendicular to KH vortices have larger growth rates, setting the direction of the disturbance to be perpendicular to the KH waves as shown in Eq.(3). x, y, z [km] are coordinates and λ [km] is the wavelength of the disturbance. $\lambda = 20, 10, 6.7, 5, 4, 2, 1.3, 1, 0.8, 0.67, 0.33$ km were investigated on S_{small} and $S_{small,hires}$ for the resolution impacts on the sensitivity analysis, and $\lambda = 80, 40, 20, 10, 6.7, 5, 4, 2, 1.3, 1, 0.8, 0.67, 0.33$ km were investigated on S_{large} for the domain width impact. We considered 10^{-5}, 10^{-6} and 10^{-7} for the amplitude of the disturbance ε to also investigate its impact on the results.

$$u(x,y,z,t=800) = \text{baseflow}(t=800) + \varepsilon \sin(2\pi(x-y)/\lambda) \tag{3}$$

The wavenumber sensitivity to the energy growth on KH vortices simulated by S_{small} is shown in Figure 8. Except for the growth of $\lambda = 0.33$ km disturbance that cannot be captured by the 0.067 km resolution, the rest of the disturbances

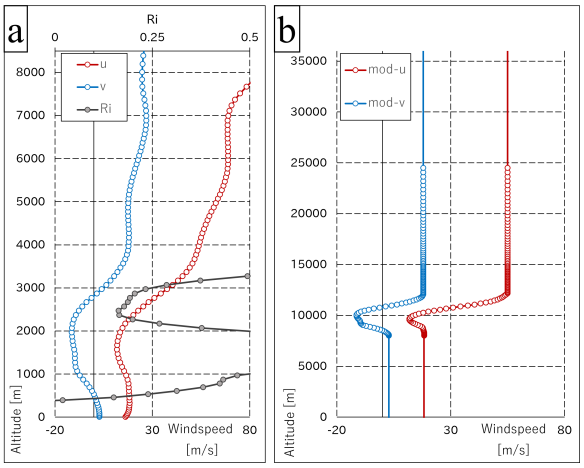

Figure 5. (a) The wind profile averaged in the region A (Fig. 4a) and calculated Richardson number, and (b) The same wind profiles except for having only the strong shear region.

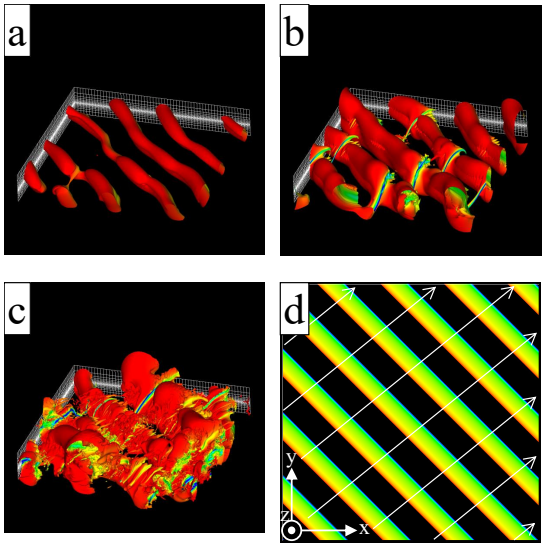

Figure 6. (a)-(c) Time history of iso-vertical wind surfaces, and (d) comparison of KH vortices and the shear vector. KH waves are visualized by 3.3 m/s iso-surface of vertical wind speed colored by pressure visualizes.

have the positive growth rates, whereas the disturbance with the lowest wavenumber ($\lambda = 20$ km) shows the fastest growth. Compared with the plots in Fig. 9, there seems to be no impact due to the difference in grid resolution.

The wavelength response behaves differently at wavelength larger than $\lambda = 20$ km. Fig.10 shows the responses on S_{large} grid and the same as in Fig.8 for wavelengths smaller than $\lambda = 20$km. For $\lambda = 40$ and 80 km, the disturbances grow with damped oscillation and stay relatively small, which is different from other monotonically increasing disturbances. We can also see the small oscillation for $\lambda = 20$ km response (Figs. 8,9 and 10).

Figure 11 shows energy growths at different initial disturbance amplitudes on S_{large} grid. Difference in amplitudes seems to have small sensitivity on the growth as 10^{-7} plots shows slightly larger energy than other amplitudes.

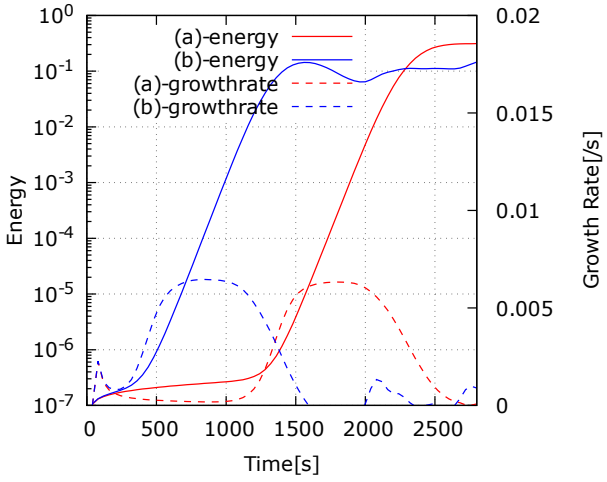

Figure 7. The energy growths and growth rates of KH vortices induced using (a) white noise and (b) sinusoidal disturbance.

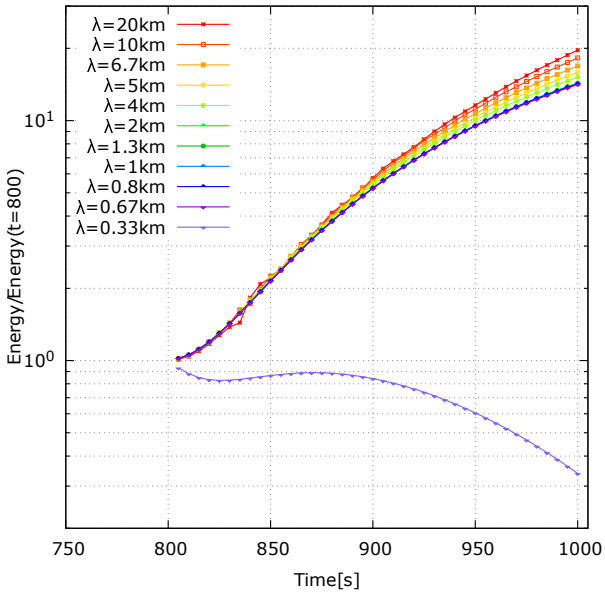

Figure 8. Wavenumber sensitivity on S_{small} simulations

CONCLUSIONS

In this study, we focused on the energy growth of vertical disturbance to the baseflow KH vortices. The results suggested that the disturbance with a wavelength near 20 km gave the largest growth. We confirm this wavelength corresponds to the interval of KH vortices bifurcation in the original simulation (Fig.6(a-c)), whose intervals are approximately 20-40 km.

We have not explained the reason why the disturbances at $\lambda > 20$ km and $\lambda < 20$ km behave differently. At $\lambda < 20$ km, the energy grows monotonically, but at $\lambda > 20$ km, the energy grows with damped oscillation. We will further investigate the growing process and report the results at the conference.

ACKNOWLEDGEMENTS

ASUCA simulations are supported by "Program for Promoting Researches on the Supercomputer Fugaku" and use computational resources of Supercomputer Fugaku provided by the RIKEN Center for Computational Science. We thank Japan Airlines for permission to use the JAL PIREP.

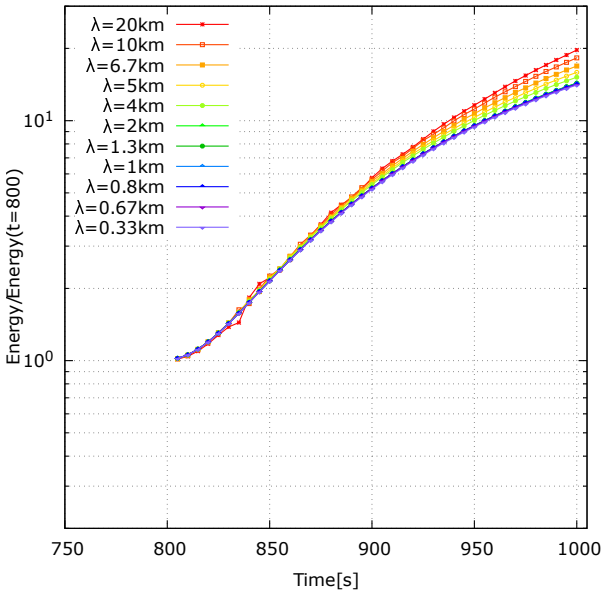

Figure 9. Wavenumber sensitivity on $S_{small,hires}$ simulations

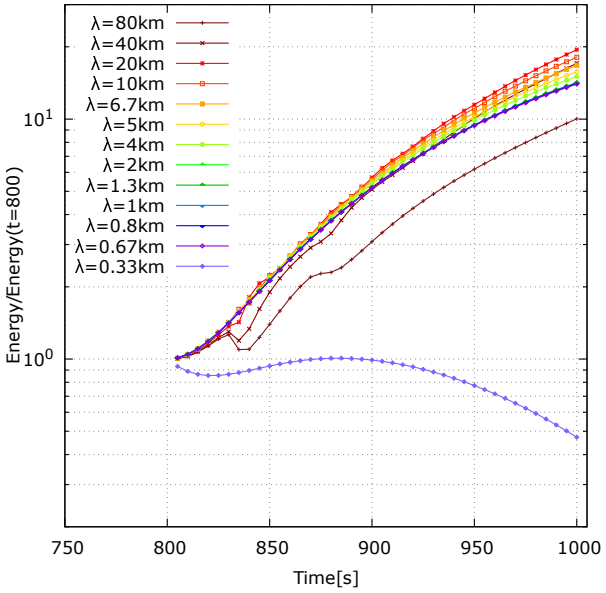

Figure 10. Wavenumber sensitivity on S_{large} simulations

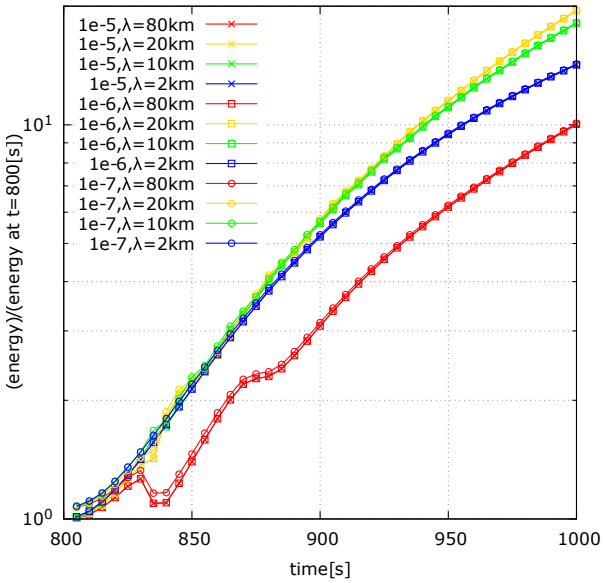

Figure 11. Amplitude of disturbance influence on S_{large} simulations

REFERENCES

Bernal, L. P. & Roshko, A. 1986 Streamwise vortex structure in plane mixing layers. *Journal of Fluid Mechanics* **170**, 499–525.

Goto, S., Saito Y. & Kawahara, G. 2017 Hierarchy of antiparallel vortex tubes in spatially periodic turbulence at high reynolds numbers. *Phys. Rev. Fluids* **2**, 064603.

JMA 2019 Outline of the operational numerical weather prediction at the japan meteorological agency. Technical report. Japan Meteorological Agency, Tokyo, Japan.

Kang, W. & Xu, L. 2012 Optimal placement of mobile sensors for data assimilations. *Tellus A: Dynamic Meteorology and Oceanography* **64** (1), 17133.

Kim, Jung-Hoon & Chun, Hye-Yeong 2010 A numerical study of clear-air turbulence (cat) encounters over south korea on 2 april 2007. *Journal of Applied Meteorology and Climatology* **49** (12), 2381 – 2403.

Lele, Sanjiva K. 1992 Compact finite difference schemes with spectral-like resolution. *Journal of Computational Physics* **103** (1), 16–42.

Liu, Junjie & Kalnay, Eugenia 2008 Estimating observation impact without adjoint model in an ensemble kalman filter. *Quarterly Journal of the Royal Meteorological Society* **134** (634), 1327–1335.

Mack, Christoph J., Schmid, Peter J. & Sesterhenn, Jorn L. 2008 Global stability of swept flow around a parabolic body: Connecting attachment-line and crossflow modes. *Journal of Fluid Mechanics* **611**, 205–214.

Pierrehumbert, R. T. & Widnall, S. E. 1982 The two- and three-dimensional instabilities of a spatially periodic shear layer. *Journal of Fluid Mechanics* **114**, 59–82.

Roberto, B., Carla, C., Graeme, K. & Jean-Noël, T. 2007 The value of observations. ii: The value of observations located in singular-vector-based target areas. *Quarterly Journal of the Royal Meteorological Society* **133** (628), 1817–1832.

Shibata, N. 1968 Turbulence in the lower layer. *Tenki* **15** (5), 201–209.

Shu, C. & Osher, S. 1988 Efficient implementation of essentially non-oscillatory shock-capturing schemes. *Journal of Computational Physics* **77** (2), 439–471.

Tomine, K., Wakamatsu, S. & Abe, S. 1987 Numerical simulation of a clear air turbulence. *Tenki* **34** (10), 625–631.

Toth, Z. & Kalnay, E. 1993 Ensemble forecasting at nmc: The generation of perturbations. *Bulletin of the American Meteorological Society* **74** (12), 2317–2330.

Trier, Stanley B., Sharman, Robert D. & Lane, Todd P. 2012 Influences of moist convection on a cold-season outbreak of clear-air turbulence (cat). *Monthly Weather Review* **140** (8), 2477 – 2496.

Trier, Stanley B., Sharman, Robert D., Muñoz-Esparza, Domingo & Lane, Todd P. 2020 Environment and mechanisms of severe turbulence in a midlatitude cyclone. *Journal of the Atmospheric Sciences* **77** (11), 3869 – 3889.

Yoshimura, R., Yakeno, A., Misaka, T. & Obayashi, S. 2020 Application of observability gramian to targeted observation in wrf data assimilation. *Tellus A: Dynamic Meteorology and Oceanography* **72** (1), 1–11.